CANCER

Targeting cancer-associated fibroblasts for real-time intraoperative tumor identification with a spray-on fluorescent probe

Riley J. Deutsch-Williams[1], Yuxuan Xie[2,3], Zachary Rabinowitz[1], Marie Goemans[1], Pratyaksha Wirapati[3,4], Claudio Vinegoni[1,5], Jonathan CT Carlson[1], Mikael Pittet[2,3,6,4], Ralph Weissleder[1,5,7]*

Surgical tumor resection is often the only curative option for the nearly 20 million newly diagnosed patients with cancer every year. Fluorescence-guided surgery techniques are being developed in an effort to improve margin detection and surgical resection outcomes, with several systemically administered imaging agents having gained clinical approval. However, it has been challenging to overcome limited margin contrast with current approaches and to navigate procedural complexities of intravenous contrast delivery. We hypothesized that "spray-on probes" with specificity for fibroblast activation protein alpha in peritumoral fibroblasts could improve fluorescence-guided surgery, detect smaller tumors, improve imaging accuracy, and reduce the amount of times a patient is hospitalized. We show that this strategy increases achievable tumor margin contrast by 5- to 10-fold and detects even microscopic cancer deposits. These improvements have the potential to transform patient outcomes by enabling more accurate cancer surgeries, reducing the number of follow-up surgeries, and leading to personalized treatment plans.

INTRODUCTION

Every year, nearly 20 million patients worldwide are newly diagnosed with cancer. For solid tumors, surgical removal is often the first option. Yet, during surgery, it can be difficult to tell where a tumor ends and healthy tissue begins because of a lack of contrast. For example, in breast cancer, rates of residual cancer following initially negative lumpectomy margins have been shown to exceed 40% in some studies (*1*). The main challenge in prostate cancer is complete cancer excision with the preservation of continence and erectile function. Positive margins still occur in up to 35% of cases.

Intraoperative imaging with light, ultrasound, x-ray, ɣ-ray, or magnetic resonance imaging has been used to enhance margin detection. Fluorescence-guided surgery (FGS) in particular represents a newer approach, using a combination of injectable fluorescent-imaging probes with specialized detection systems to visualize cancers and their margins more accurately. Over the past 25 years, many different imaging agents have been described (*2*–*8*). Despite these efforts, it has been challenging to (i) overcome limited tumor-to-background ratios (TBRs) with current FGS approaches, (ii) navigate the procedural complexities with intravenously injected probes (careful planning of injection times before surgery, field contamination if probes are still circulating at the time of operation, and targeting of heterogeneous tumor cells rather than host response), and (iii) reduce the adverse event rate of ~20% of patients when receiving systemic administration (*9*).

An alternative to intravenously injected imaging probes are topically applied ones. In theory, this can improve FGS, allow one to find smaller tumors (higher TBR), enable new functionalities, improve imaging accuracy and speed, reduce the dose, and diminish systemic side effects. In prior research, we had identified a fluorescent imaging probe targeting fibroblast activation protein alpha (FAP) (*10*). FAP has been shown to be a ubiquitous target in many different cancers (*11*–*14*), and FAP–positron emission tomography imaging is being increasingly used clinically. Targeting the host response (e.g., FAP in tumor-associated fibroblast) assures strong target expression across different cancer types (*15*), avoiding the highly heterogenous target expression of cancer cells (e.g., what is usually probed for with tumor markers like anti–epidermal growth factor receptor and anti–carcinoembryonic antigen).

To show proof of principle of FAP imaging, the prior lead probe [FAP-Targeting Fluorophore-BODIPY TMR (FTF-BODIPY-TMR)] identified by a screen was still injected intravenously and subject to the same limitations as other small imaging agents. To speed up clinical decision making, improve local contrast, and minimize systemic side effects, we wondered whether topical administration of such an imaging agent would be feasible. This was far from obvious as questions arose of target adherence, the ability to wash away unbound imaging agent, and the best procedures to optimize delivery and wash-steps while minimizing procedural complexity. We found that simple spray-on of the FTF-BODIPY-TMR by itself did not work well as there was limited tissue adherence, requiring reformulation. We therefore explored and optimized formulations and procedures for spray-on probes (SOPs). We unexpectedly show that certain SOP, formulations, and technologies can deliver extraordinarily high TBR (much higher than with systemic injections) at a fraction of the dose and in different cancer models. We further developed computational approaches to achieve real-time margin assessment using conventional machine learning methods. We term this new method of precision tumor removal through spray-on surgery "SOS" and optimized "SOP."

[1]Center for Systems Biology, Massachusetts General Hospital, 185 Cambridge St., CPZN 5206, Boston, MA 02114, USA. [2]Department of Pathology and Immunology and Center for Translational Oncohaematology Research, University of Geneva, Geneva, Switzerland. [3]AGORA Cancer Research Center and Swiss Cancer Center Leman, Lausanne, Switzerland. [4]Department of Oncology, Geneva University Hospitals, Geneva, Switzerland. [5]Department of Radiology, Massachusetts General Hospital, 32 Fruit St., Boston, MA 02114, USA. [6]Ludwig Institute for Cancer Research, Lausanne, Switzerland. [7]Department of Systems Biology, Harvard Medical School, 200 Longwood Ave., Boston, MA 02115, USA.
*Corresponding author. Email: rweissleder@mgh.harvard.edu

RESULTS

Synthesis of lead SOP probe

A small number of FAP-targeted imaging probes have been described in the literature, but many were developed for intravenous use or enzymatic assays (*10*, *16*, *17*). To determine whether some of these probes could be used for topical application, we screened a number of different conjugates in the visible range. Unexpectedly, we found that only one probe [FTF-BODIPY-TMR (*10*)] worked well for topical administration. For this reason, we scaled up the synthesis from a commercially available FAP-IN-2 precursor with a free piperazine for coupling. This was reacted with an *N*-hydroxysuccinimide (NHS)–activated BODIPY TMR-fluorescent dye in a single-step reaction to achieve 82% yield of the desired product (Fig. 1B). Liquid chromatography–mass spectrometry (LC-MS) were used to assess final purity and the generation of the desired product. The purified SOP probe eluted at 1.2 min in a single narrow peak consisting of the expected product as measured in MS (Fig. 1C). We also performed nuclear magnetic resonance (NMR) spectroscopy to confirm the expected structures: The ^{1}H NMR aromatic region [δ 6.5 to 9.5 parts per million (ppm)] of the SOP contained signature peaks for the quinoline moiety of FAP-IN-2 and for BODIPY-TMR (fig. S1). Last, absorbance and fluorescence spectroscopy were performed, confirming that the SOP probe maintained an excitation peak at 550 nm and an emission peak at 579 nm (Fig. 1D). Before testing on live tissue, we also performed an MTT cell viability assay to determine any cytotoxic effector FTF-BODIPY-TMR. Briefly, NIH-3T3 cells were treated with varying concentrations of probe for 2 min before a rinse and incubation for 72 hours. Cells were then treated with PrestoBlue for 60 min and absorbance measurements were collected at 570 nm. We found that cell viability remained above 94% for all concentrations, suggesting negligible effect of the probe on live cells (Fig. 1E).

Optimization of a clinically feasible staining protocol

In designing a method for generating tumor-specific contrast from an SOP, we sought to optimize several variables, including the actual formulation for spray-on topical administration, probe concentration, stain time, and wash time. We systematically optimized these four variables using fresh murine thick tissue sections as outlined in Fig. 2A. Briefly, green fluorescent protein (GFP)–tagged 4T1 mammary tumors, healthy liver, and gonadal fat pad were excised and cut into 300-μm sections for serial optimization of stain time, stain concentration, wash time, and spray formulation.

We first determined whether the SOP probe could achieve tumor-specific contrast when applied topically within a surgically

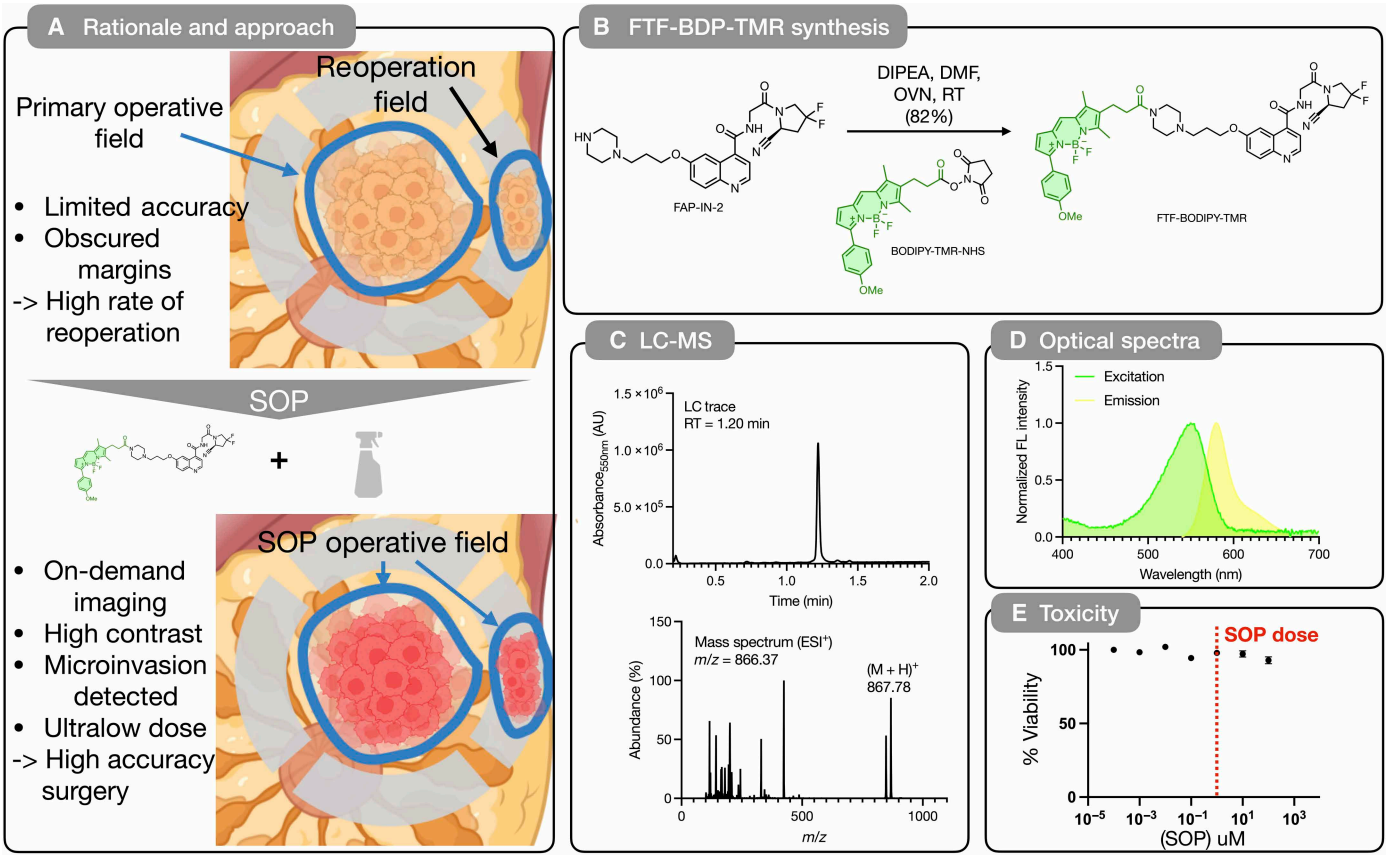

Fig. 1. Overview of SOP concept and design. (**A**) Overview of rationale and clinical need for an SOP. During conventional resection of primary tumor lumps, the lateral margins often have low TBR, resulting in missed cancers. With SOP probes, the TBR is vastly enhanced, leading to improved margin detection. Created in BioRender. Deutsch, R. (2025) https://BioRender.com/c2jv1aj. (**B**) Synthetic scheme for conjugating the FAP ligand with a BODIPY-TMR via an NHS-activated ester, resulting in FTF-BODIPY-TMR. (**C**) LC-MS traces for the purified FTF-BODIPY-TMR compound. (**D**) Excitation and emission spectra of the product compound. (**E**) In vitro concentration–dependent toxicity of FTF-BODIPY-TMR. Cells were treated with probe for 2 min before incubating for 72 hours in media. Red vertical line indicates concentration used for SOP imaging. AU, arbitrary units.

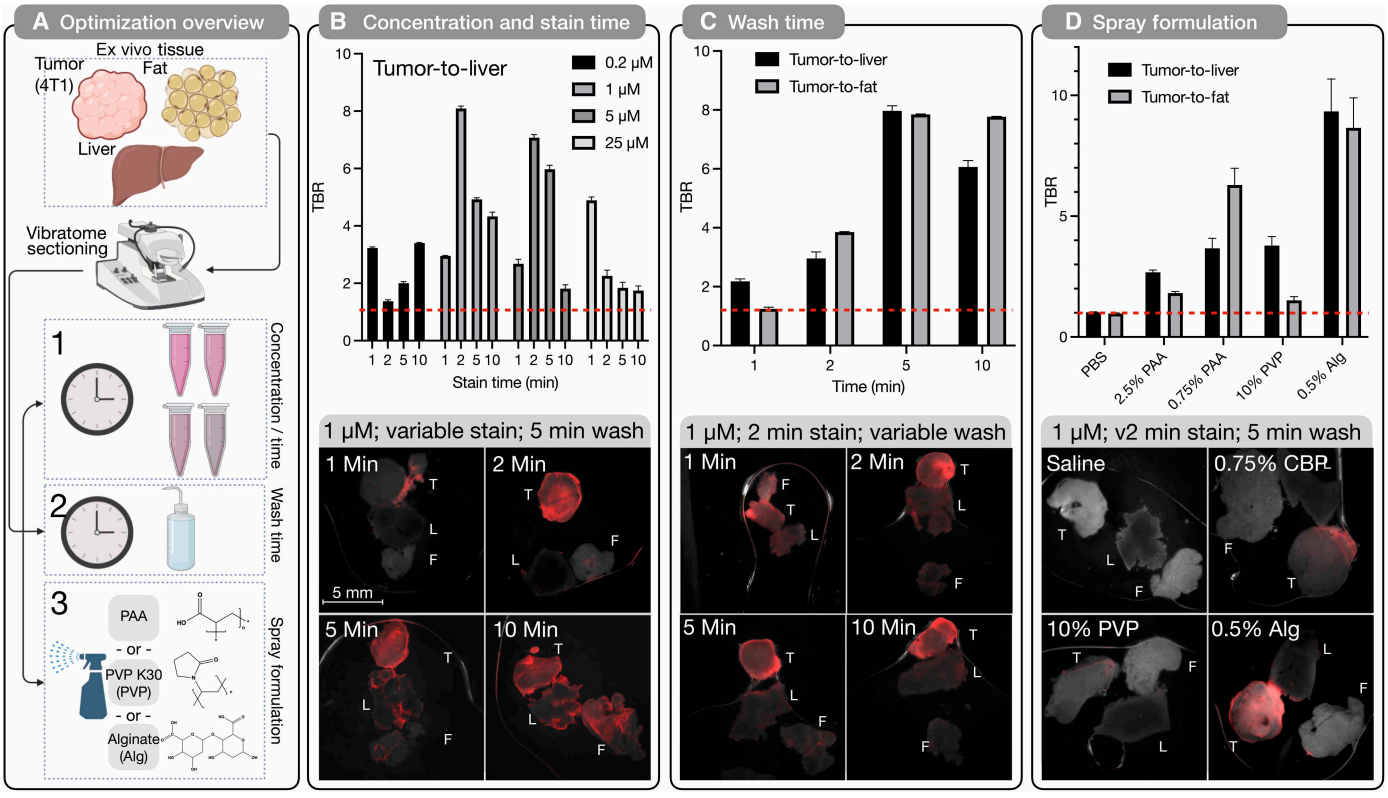

Fig. 2. Ex vivo optimization of FTF-BODIPY-TMR spray on probes. (**A**) Experimental overview. Briefly, fresh tissue sections of murine tumor (4T1), fat, and liver were used to optimize probe concentrations, stain/wash times, and spray formulation. Three formulations were tested containing PAA, PVP K30 (PVP), or alginate (Alg). Created in BioRender. Deutsch, R. (2025) https://BioRender.com/4kl35o0. (**B**) Mean tumor-to-background measurements for tumor-to-liver contrast as a function of both probe concentration and stain time with tissue submerged in probe solution. Tumor-to-fat results are shown in fig. S2. Representative images show results of a 1 µM stain concentration, variable stain times, and a 5-min wash. (**C**) Mean tumor-to-background measurements for tumor-to-liver and tumor-to-fat as a function of wash time with a fixed 1 µM stain concentration and 2-min stain time with tissue submerged in probe solution. Representative images included. (**D**) Mean tumor-to-background measurements for tumor-to-liver and tumor-to-fat as a function of spray formulation with a fixed 1 µM stain concentration, 2-min stain time, and 5-min wash. Formulations tested included PBS only, 2.5% PAA, 0.75% PAA, 10% PVP, and 0.5% alginate. For (B) to (D) $n = 3$, analysis of variance (ANOVA) with a Tukey's post hoc test. Red line indicates TBR = 1 (no contrast). Representative images in each panel show tumor (T), liver (L), and fat (F) with probe signal in (red) superimposed on bright-field images.

relevant time frame (<10 min). Tissue sections were submerged in SOP solutions of various concentrations and incubated for variable amounts of time. After a 5-min wash, tissues were imaged with a wide-field imaging system. Mean intensity values for tumor, liver, and fat tissues were measured and used to calculate TBRs. We observed that when compared to liver tissue tumor, contrast was highest with a stain time of 2 min and a concentration of 1 µM (Fig. 2B). While the absolute intensities of tumor tissue was higher in longer stain conditions (5 and 10 min), these conditions also led to an increase in nonspecific staining that could not wash out in 5 min. The strong signal of the 2-min stain combined with the near-zero accumulation of nonspecific stain led to the high TBRs reported. These same trend held for tumor-to-fat ratios (fig. S2).

We next sought to determine the minimum wash time necessary to achieve an optimal TBR in the ex vivo tissue model. All tissues were stained with 1 µM SOP for 2 min before washing for a variable amount of time. Figure 2C illustrates the relationship between TBR and wash time for both liver and fat (tumor-to-liver and tumor-to-fat ratios shown). An increase in TBR was observed for a 5-min wash compared to a 1- or a 2-min wash ($P < 0.5$), however, not between 5 and 10 min. This suggests that after 5 min of washing, most nonspecific dye has been removed. Representative images in Fig. 2C further highlight how changes in TBR can be attributed to a decrease in probe signal in liver (L) and fat (F) tissues (shown in red), and not a change in tumor (T) signal strength.

We further explored the feasibility of spraying our probe as an atomized mist onto the tissue surface using different commercial atomizers (fig. S3A). We selected a spray device that produced a fine aerosol mist capable of covering the largest tissue area (fig. S3, B and C). When a formulation of dye and saline alone was sprayed onto the tissue, it was observed that most of the applied volume ran off the tissue surface and pooled underneath, producing no appreciable contrast between tumor and normal tissues (Fig. 2D). To resolve this, we tested various polymer-based formulations, with substances that have previously been shown to increase viscosity, tissue adhesion, or hydrogel formation (*18*). Specifically, we tested formulations with polyacrylic acid (PAA, 2.5 or 0.75% w/v), polyvinylpyrrolidone (PVP, 10% w/v), and alginate (Alg, 0.5% w/v). While PAA and PVP both increased the viscosity of the probe solution, they no longer allowed the formation of an atomized mist, resulting in nonuniform coverage without achieving tissue adhesion (fig. S4, A and B). Conversely, alginate is known to form a hydrogel in the presence of calcium ions and

to de-gel in the presence of a calcium chelator such as EDTA. Calcium alginate is commonly used in surgical dressings, and 10% calcium solutions are approved for a variety of conditions. By first spraying with a calcium chloride solution (3% w/v) and then with an alginate-containing SOP, a gel was formed to trap the probe uniformly across the tissue surface. Following a 2-min stain, a 3% EDTA solution was applied to the hydrogel to depolymerize the gel before a standard 5-min wash with phosphate-buffered saline (PBS). A significant increase in TBR against both normal liver (TBR = 9.3 ± 1.3; $P < 0.05$) and fat (TBR = 8.7 ± 1.2; $P < 0.05$) was observed (Fig. 2D). On the basis of these results, we performed subsequent tissue imaging with a pretreatment of calcium chloride, 1 μM SOP formulated with 0.5% alginate, a 2-min stain time, a 5-min wash, and a wash with EDTA.

SOP enables automatic segmentation of tumor regions

We next applied the optimized SOP protocol to detect margins in a variety of murine solid tumor models. Specifically, we imaged MC38 colorectal, 4T1 mammary, KPCY 2838c3 pancreatic, and B16 F10 melanoma tumors (all tagged with GFP) along with normal mammary, liver, lung, colon, and uterine tissue. With this set of images, we performed a set of preprocessing steps, implemented a pixel-wise *k*-means clustering with three clusters, and used the highest intensity cluster to outline tumor regions and estimate margins (Fig. 3A). *K*-means clustering was performed on the aggregate of all stained tumor data. As seen in Fig. 3B, the cluster regions can be associated with SOP^+ tumor regions, tumor periphery, and background tissue. When the same cluster centroids are applied to images of normal tissue, >99% of pixels are binned as nontumor background, and no pixels are labeled as tumor. Tumor segmentation masks were generated from the pixels within the SOP^+ tumor cluster, and masks were subsequently used to generate 1- and 3-mm margins. To assess the accuracy of our segmentation approach, ground truth labels for tumor regions were generated via an intensity-based thresholding of the fluorescent tumor signal. Quantification of imaging and segmentation results are summarized in Fig. 3C. Each tumor achieved a mean TBR of between 7.3 and 11.8 when compared to surrounding tissue but maximum TBR values of 20 to 30. To assess the ability of the SOP probe and segmentation algorithm to successfully delineate tumor regions, ground truth masks were generated by applying an Otsu's thresholding to the tumor fluorescent protein signal images. Accuracy of FTF-based segmentation was quantified via Jaccard index and Dice scores. Each tumor type achieved a Dice score > 0.8, indicating successful segmentation, with best performance seen in the MC38 and KPCY 2838c3 tumor models (Dice score > 0.93).

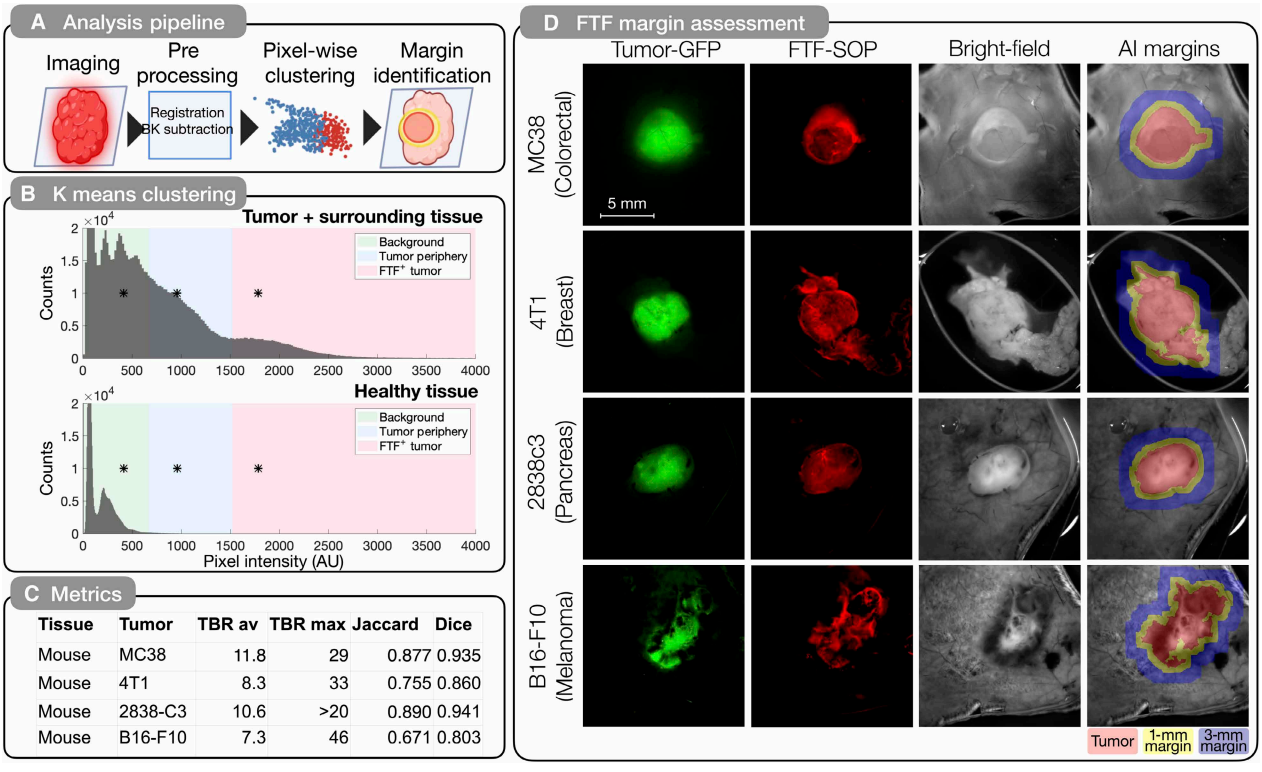

Tissue	Tumor	TBR av	TBR max	Jaccard	Dice
Mouse	MC38	11.8	29	0.877	0.935
Mouse	4T1	8.3	33	0.755	0.860
Mouse	2838-C3	10.6	>20	0.890	0.941
Mouse	B16-F10	7.3	46	0.671	0.803

Fig. 3. SOP staining enables machine learning–based tumor identification across multiple tumor types. (**A**) Analytical pipeline used for automatic tumor segmentation and margin delineation. All images underwent coregistration and background subtraction, followed by a *k*-means pixel-wise clustering to generate tumor segmentation masks. Created in BioRender. Deutsch, R. (2025) https://BioRender.com/jiunqtf. (**B**) Generation of tumor-specific *k*-means clusters. Images of SOP-stained MC38, 4T1, 2838c3, and B16 F10 tumors and surrounding tissue combined into a cumulative histogram for cluster analysis. Cluster centroids are illustrated with an "✳", and cluster bins are delineated as green, background; blue, peripheral tissue; red, tumor. The same clusters were applied to cumulative histogram of healthy tissues shown in fig. S3. (**C**) Quantitative image metrics per tumor type including average TBR (mean of entire tumor region); maximum TBR (top 10% of tumor pixel intensities); Jaccard index; and Dice score. Jaccard indices and Dice scores were calculated with thresholded tumor-GFP signal. (**D**) Representative images of each tumor type including tumor-intrinsic GFP signal, FTF-SOP signal, bright-field imaging, and automatic margin overlays. For overlays, three regions are shown indicating tumor region (red), a 1-mm margin (yellow), and a 3-mm margin (blue).

Representative images in Fig. 3D include tumor fluorescent protein signal, SOP signal, bright field, and tumor margin overlays for each of the four tumor types. Margin overlay widths were selected on the basis of clinical recommendations for breast conserving surgeries (*19*) and could be adjusted on a personalized basis. In contrast, images of stained normal tissues reveal no detectable SOP or GFP signal, with an average TBR of 15.3 across all normal tissue types compared to 4T1 tumor (fig. S4). As can be seen, the SOP signal in each scenario is largely concordant with the fluorescent protein signal. We noticed that the SOP-positive regions in the 4T1 mammary tumor expanded beyond the fluorescent protein signal by surface-wide field imaging. While this contributes to the lower Jaccard and Dice scores for this model, we were curious whether, microscopically, this represented a false-positive signal or not and thus performed additional cellular experiments.

Cellular imaging confirms SOP accumulation around microscopic tumor clusters

Using confocal microscopy, we explored the single-cell distribution of SOP probe within tumors and adjacent resection tissues. 4T1-GFP tumors were resected, stained as previously described, and imaged with both a wide-field and confocal microscope. We observed cellular SOP signal with confocal staining patterns comparable to wide-field imaging. When overlaid with the tumor-specific GFP signal, it became obvious that there was strong concordance between the two signal types, but it was still possible to observe regions of SOP signal distant from the bulk tumor. To explore the nature of these SOP^+ regions, we performed higher confocal resolution imaging. We found GFP-positive tumor cells and microscopic tumor deposits in all SOP^+ regions (images i to iii in Fig. 4B). After imaging 40 fields of view (FOVs) across eight tumors (fig. S6, A and B), we found that SOP^+ signal indicated the presence of tumor cells in 100% of images (fig. S6C). This suggests that SOPs can enable the macroscopic identification of tissue regions containing microscopic tumor cell clusters, making the technology competitive with other fluorescent probes. Note that, for comparison, clinical imaging agents often only achieve a TBR of 4 to 6 (fig. S6D).

Using antibody costains, we further characterized the location and cell types of SOP^+ cells. Analysis of confocal sections, taken in 10-μm steps, allowed for quantification of staining depth. SOP signal intensity decreased to 50% of peak intensity 30 μm beneath the tissue surface, indicating that the macroscopic signal is generated by these superficial cell layers, as expected (Fig. 4C). By costaining with an anti–CD45-AF647 antibody, it was possible to see that SOP signal originated from a distinct cell population from CD45 immune cells at both macroscopic and microscopic resolutions [coefficient of determination (R^2) = 0.35, $P < 0.05$]. Conversely, costaining with an anti–FAP-AF647 antibody indicated strong correlation between

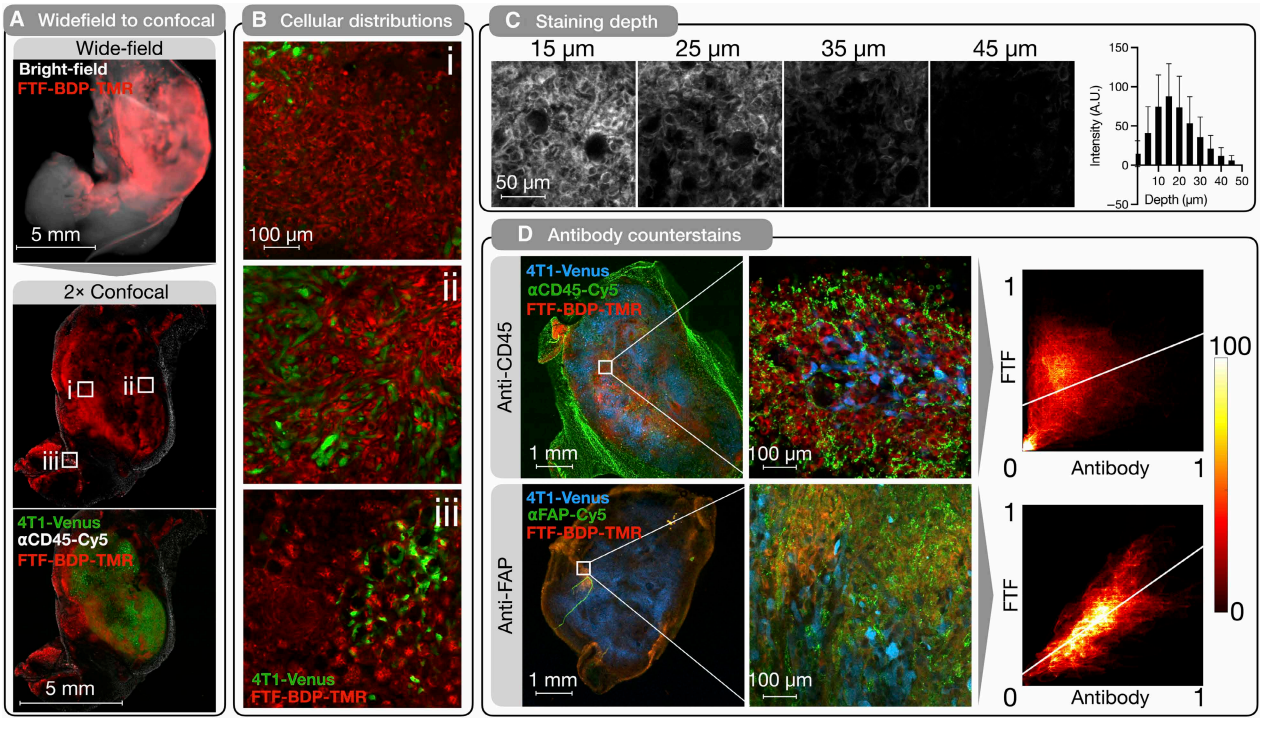

Fig. 4. Confocal imaging of SOP distributions at single-cell resolutions. (**A**) Correlative wide-field and confocal imaging of a 4T1 mammary tumor. For wide-field imaging, merged SOP and bright-field data are shown. For confocal imaging at 2× magnification, tumor-GFP signal is shown in green, SOP signal is shown in red, and anti-CD45 antibody stain is included in grayscale to delineate border of peripheral tissue. Three demonstrative regions of interest are selected (i to iii) for high-resolution analysis. (**B**) High-resolution (20×) imaging of SOP-labeled tumor. Regions selected illustrate high-density FAP^+ cells (i), interspersed tumor and FAP^+ cells (ii), and microscopic tumor deposits with surrounding FAP^+ cells (iii). For extended results on improved margin detection, see fig. S6. (**C**) Analysis of confocal z-stacks reveals depth of probe penetration to be 25 μm. Images were collected in steps of 5 μm. Graph depicts average image intensity at each step. (**D**) Correlation of SOP signal with anti-CD45 (top) or anti-FAP antibody. Images were acquired at both 2× and 20× magnification. Two-dimensional scatter plots were generated for each image set to quantify correlation between SOP and AB signal. Linear regression was performed, and correlation was assessed with a Pearson's correlation coefficient.

antibody and probe signal as indicated by orange regions (overlap of red and green colormaps) at both macroscopic and microscopic resolutions ($R^2 = 0.73$, $P < 0.05$) (Fig. 4D). In total, these findings suggest that SOPs uniquely label FAP$^+$ cancer–associated fibroblasts and indicate the presence of tumor cells.

Demonstration of fluorescence SOS in a preclinical model

The SOS method was next tested in the more complex intraoperative setting in live mice. To enable this, we designed a custom wide-field imaging system with the core optics of a dissection microscope to provide surgically relevant resolutions at a working distance amenable to real-time FGS (fig. S7A). This system was characterized as having a 31-μm lateral resolution with a 20 mm–by–17 mm FOV, or a 14-μm lateral resolution with a 5.1 mm–by–4.3 mm FOV (fig. S7, B and C).

On the day of surgery, the abdominal skin above right mammary tumor was removed to expose the tumor-bearing gland. White-light reflectance and fluorescence images were acquired at each surgical step (prestain, poststain, postexcision, and restained) and are summarized in Fig. 5. The exposed tissue field was stained with SOP as previously validated. After staining, imaging was performed again, and the *k*-means–based segmentation algorithm was used to identify tumor regions and surrounding margins. On this basis, the tumor region was resected, ensuring that all SOP$^+$ tissue was removed from the surgical field. To ensure that no residual disease remained, the site was restained with SOP and imaged to confirm that the tumor had been successfully resected. Each iterative round of staining, imaging, and excision took approximately 15 min. We further validated the efficacy of the SOP probes for FGS using a GFP-labeled 4T1 tumor model. We show that the absence of SOP signal following tumor resection corresponds to an absence of GFP signal, suggesting a successful complete resection (fig. S8). Further, when we restain the margin-side of the resected tumor, an absence of both GFP and SOP fluorescence indicates that a sufficiently wide margin of healthy tissue was removed.

Spatial transcriptomic profiling reveals FAP as a pan-tumor marker for human cancer

With strong evidence that the SOP method generated tumor-specific contrast in a variety of tumor models, we explored the translation to human tissues. We first asked whether FAP expression is broadly conserved across a number of tumor types. To answer this, we performed analyses of published high-quality single-cell RNA sequencing datasets (*20*–*31*). In total, we analyzed data from 353 patients across eight different cancer types (Fig. 6A). When looking at FAP expression levels across different cell types for all patients, we found FAP-expressing fibroblasts to be highest in fibroblasts and prevalent in all patients (Fig. 6B). Further, when these data are parsed by tumor type, we see that FAP-expressing fibroblasts are widely found across all cancer types, supporting the use of the SOP as a pan-cancer marker (fig. S9). When analyzing studies consisting of both tumor and normal samples, we observed that fibroblasts from tumor tissues consistently showed higher FAP expression than those in the normal samples in colorectal, lung, and head and neck cancers (Fig. 6C).

On the basis of microscopic analysis of SOP signal distribution, we also explored the spatial relationship between tumor cells and fibroblasts by leveraging 10 publicly available human cancer visium HD datasets at 10X Genomics website [10X Genomics, Accessed 2025 (*32*)]. In human breast cancer, colorectal cancer and non–small cell cancer, we found higher FAP expression in fibroblasts typically within 500 μm of tumor cells, indicating up-regulated FAP

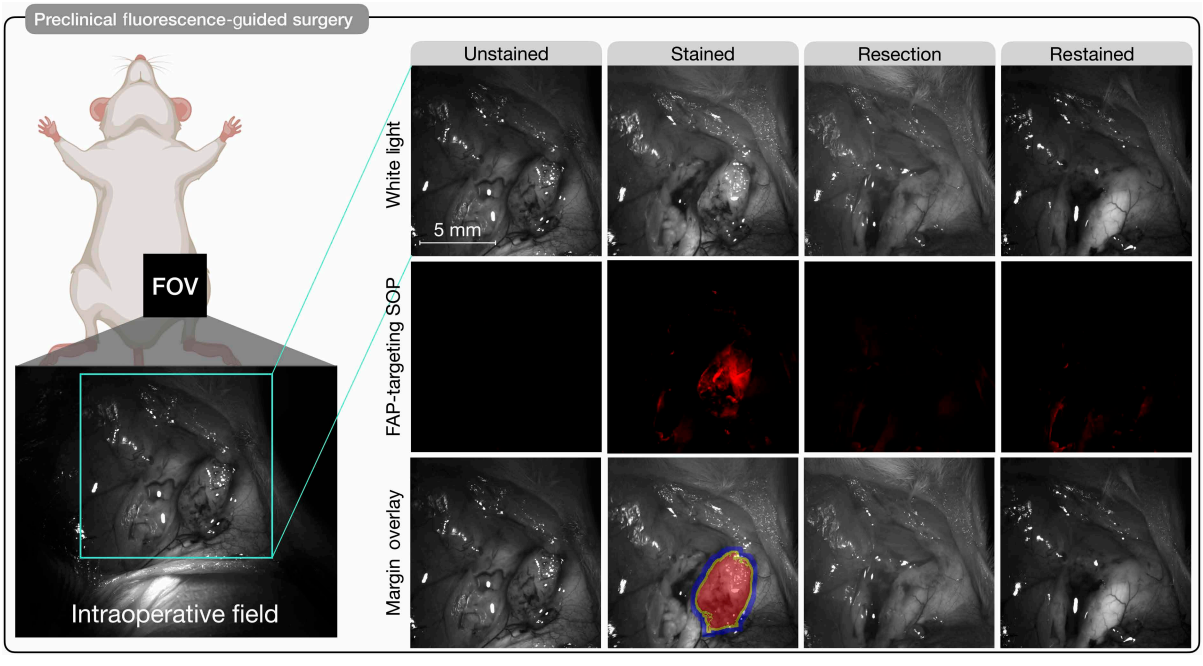

Fig. 5. SOP imaging and AI margin detection for real-time FGS. FGS was performed on an orthotopic 4T1 mammary tumor. Images of the intraoperative field were acquired before staining, poststaining, after excising the tumor, and following a restain. At each point bright-field and SOP fluorescence images were acquired. From these images, automatic image segmentation was performed to generate the margin overlay images identifying the tumor (red), a 1-mm margin (yellow), and a 3-mm margin (blue). Created in BioRender. Deutsch, R. (2025) https://BioRender.com/elbp78f.

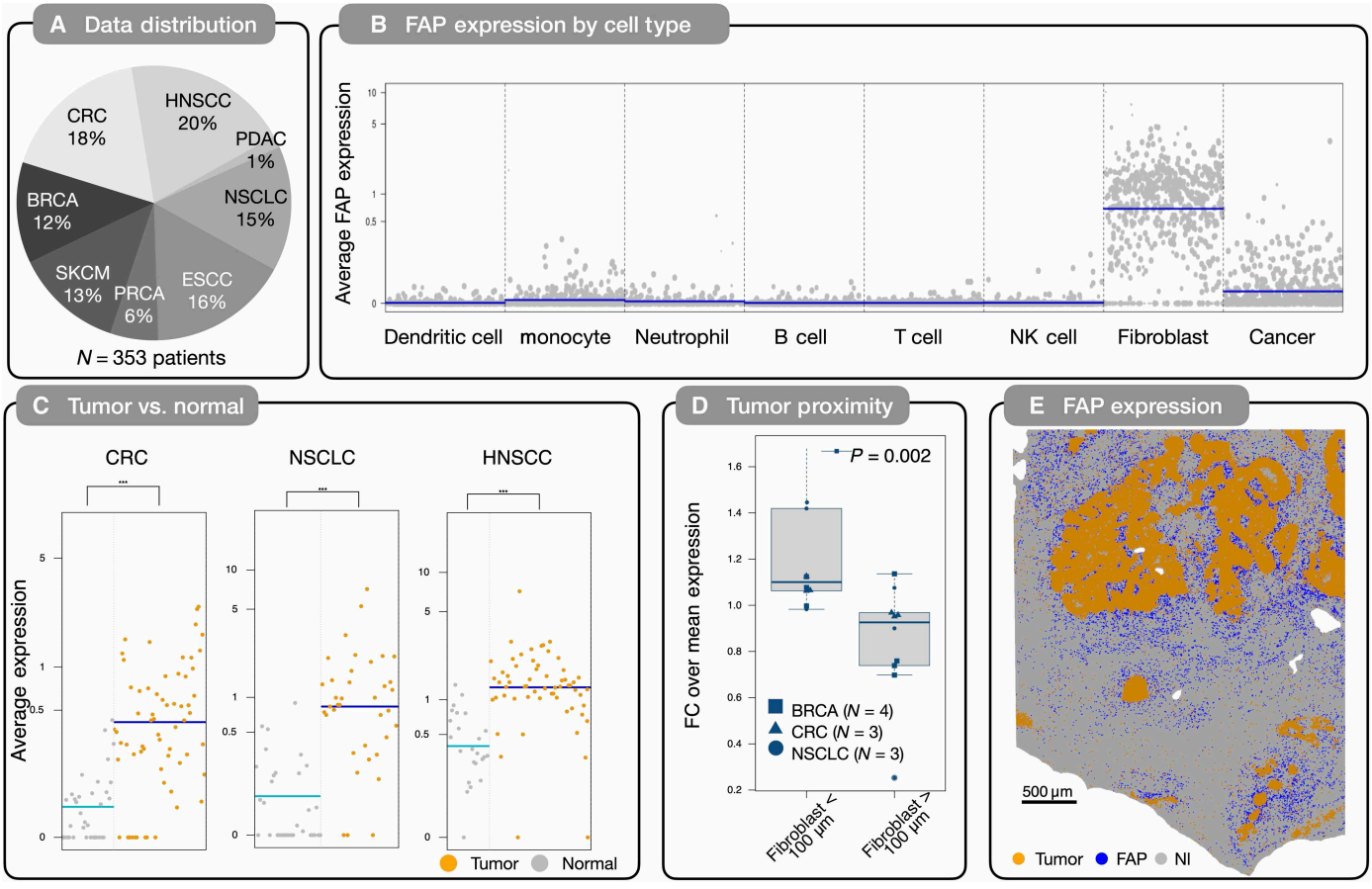

Fig. 6. Spatial transcriptomic profiling of FAP expression across multiple human cancer types. (**A**) Summary of cancer types in analyzed dataset. BRCA, breast cancer; CRC, colorectal cancer; HNSCC, head and neck squamous cell cancer; ESCC, esophageal squamous cell cancer; NSCLC, non–small cell lung cancer; PRCA, prostate cancer; SKCM, skin cutaneous melanoma; PDAC, pancreatic duct adenocarcinoma. (**B**) Average FAP expression by cell type across all patient data. Each data point represents a single patient plotted on a logarithmic scale. (**C**) Average FAP expression in normal and tumor tissues for three cancer subtypes and normal tissue. Each data point represents a single patient plotted on a logarithmic scale. ***$P < 0.05$. (**D**) FAP expression is parsed by the distance between the fibroblast and the tumor cell. Analysis performed on the following subset of patients: BRCA ($n = 4$), CRC ($n = 3$), NSCLC ($n = 3$). Statistical significance was determined with a Wilcoxon rank sum test. (**E**) Representative image of FAP$^+$ cells and their spatial relationship to tumor cells. Here, the tumor is depicted in orange, FAP$^+$ fibroblasts are depicted in blue. Note the spatial proximity of FAP$^+$ fibroblasts around tumor deposits.

levels at close tumor boundaries (Fig. 6, D and E). By calculating the Euclidean distance between fibroblasts and cancer cells, we were able to confirm that most of the fibroblasts are found within this 500-µm cutoff in human cancers and that FAP expression decreases as the distance from the tumor increases. These trends were found to be true across tumor types and are reported in fig. S10.

Supported by preclinical results and bioinformatics analysis, we also tested the SOP staining concept on core-needle biopsies. Freshly obtained liver biopsies of human adenocarcinoma ($n = 3$) were stained with the SOP protocol and counterstained with proflavine, a common nuclear stain. Confocal imaging at 2× magnification revealed SOP signal across the length of the biopsy, with distinct SOP$^+$ cells being observed throughout the entire metastatic core (Fig. 7A). After imaging, biopsies were fixed, embedded, sectioned, and stained with hematoxylin and eosin (H&E). H&E images confirmed the presence of cancerous cells across the length of the biopsy (Fig. 7B). Together, this evidence supports the feasibility of SOP staining of human tumor tissue.

DISCUSSION

While there are an abundance of systemically administered imaging probes for FGS including small molecules, nanoparticles, and biologics (*6*), most suffer from one of two shortcomings: (i) Imaging agents target a marker that is overexpressed in only a subset of cancers but are not broadly applicable as a diagnostic marker (*33*, *34*), or (ii) broadly applicable contrast agents suffer from low tumor specificity (*35*, *36*). We hypothesized that SOP containing a unique FAP-targeting fluorescent probe could dramatically improve FGS, find small tumors (higher TBR), improve imaging accuracy, reduce the number of clinical visits required of a patient, and reduce the administered dose compared with systemic administrations. The practical challenge is to develop procedures that do not add to the length of surgical procedures but actually improve them by reducing uncertainties due to higher detection accuracy. The current turnaround for intraoperative frozen sections is <20 min (*37*), while the SOP technology developed here is <10 min. Overall, these improvements have the potential to transform patient outcomes by enabling

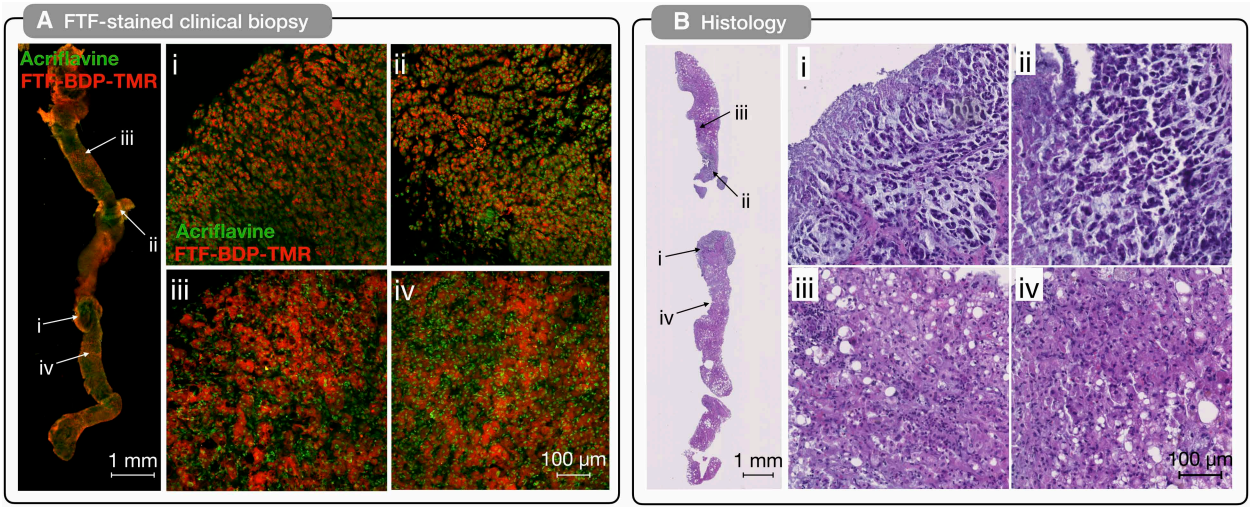

Fig. 7. Proof-of-principle spray-on experiment in a human tumor sample. (**A**) A freshly harvested human core biopsy specimen (metastatic adenocarcinoma to liver) was stained with the established SOP protocol (shown in red). In addition, the sample was counterstained for 1-min with an acriflavine nuclear stain (shown in green). Confocal imaging was performed at a 2× and 20× magnification to observe both bulk and cellular distributions of SOP signal. Regions i to iv in the 2× image correspond to regions of 20× imaging. (**B**) Confirmatory H&E staining demonstrates the presence of tumor in the entire core biopsy specimen.

more accurate cancer surgeries, personalized treatment plans, and decreasing the need for reoperations. While the concept of an SOP (Fig. 1A) is intuitive, we made several key findings necessary for the success of SOP technologies.

Choice of FAP-targeted fluorophore

The choice of the imaging agent used in SOP formulation was critical. Existing work done in the field of nuclear medicine has demonstrated the diagnostic power of targeting FAP for molecular imaging. Specifically, FAP-based nuclear imaging demonstrates high specificity for tumor tissue with remarkably low background in adjacent tissues compared to gold-standard fludeoxyglucose (*38*, *39*). In addition, radiolabeled FAP inhibitors have shown broad generalizability to a variety of tumor types (*40*). Further, we had previously synthesized a variety of FAP inhibitor–fluorophore conjugates (FTF probes) and found that not all performed equally well. We demonstrated that only a select few conjugates (two of six) could successfully target and label FAP-positive cells when injected systemically, although all of them had nanomolar affinity for FAP (*10*). We thus chose this lead candidate and formulated it into the current SOP version, containing alginate and buffers for more effective in vivo use.

Formulating for topical spray-on

We empirically found that an alginate-based spray-on formulation allows for rapid gelation of our SOP upon contact with calcium-pretreated tissue. The addition of hydrogel-forming alginate was key to ensuring that the probe remained uniformly in contact with the tissue throughout the staining period to achieve optimal tumor contrast. Medicinal sprays have experienced successful clinical translation in the fields of nasal drug delivery and wound healing. A number of biologically inert polymers, including the family of synthetic PAA-based carbomers and PVD, have been explored for their mucoadhesive properties (*18*). We found that such polymers also tend to increase the viscosity of spray formulations, affecting both droplet size and spread of spray [higher viscosity leading to larger droplets, narrower spray, and less uniformity (*41*)]. In our trials, this impact on spray performance actually resulted in worse tumor contrast. This inspired us to look into organic polymers that exhibited the ability to undergo hydrogel formation based on an external cue.

While there are a number of solutions to this including pH sensitivity, thermal sensitivity, or reaction in the presence of a copolymer (*42*), we found alginate to be the most efficacious SOP formulation. This can be attributed to the ability of alginate to rapidly gel in the presence of calcium chloride for staining and to de-gel in the presence of a calcium chelator for rinsing.

Advantages of topical over systemically injected probes

While intravenous delivery has been the standard approach for most FGS methods, there are several limitations that can be overcome with SOPs. First, intravenous delivery requires the imaging agent to be introduced many hours before the time of procedure. This adds additional planning and trips to the clinic for both the patient and the provider. In contrast, SOPs require mere minutes to generate tumor-specific contrast, making topical stains a viable option for both intraoperative settings and also for point-of-care diagnostics. Given the growing presence of well validated, low-cost fluorescence imaging systems designed for clinical use in low-resource settings (*43*–*46*), the SOP technology could be well suited to aid in the global care of cancer in a variety of disease types including cervical cancer, oral cancers, and skin cancers. Each of the aforementioned cancer types also offer established practices for topical-based contrast. During colposcopy, topical application of acetic acid or Lugol's iodine are both common for the visual identification of tumor lesions (*47*). A number of probes have been tested in oral cancer involving rinsing of the oral mucosa with stain to generate contrast (*48*). One additional challenge of intravenous delivery is that it is limited to well-vascularized tissue. For poorly vascularized tumors, this can lead to false-negative signals (*49*) and regions of necrosis can appear as false positives (*50*). While we have established a case for SOPs, there may also be a useful clinical paradigm involving the combination of intravenous delivery and SOPs. As mentioned, intravenous delivery can help to detect general tumor regions deep in tissue, while SOP offers

a potentially complementary mode of contrast that is not limited by vascular delivery and offers a higher level of sensitivity to small pockets of invasive tumor cells.

Relationship between FAP$^+$ cells and tumor cells

FAP is primarily produced by activated fibroblasts, such as mCAF. FAP levels are much lower in other fibroblast subtypes, other tissue microenvironmental cells (e.g., fat, lymphatics), or in tumor cells (Fig. 6). These observations are increasingly established and independently validated through public datasets (*20*–*31*). A key question was how the FAP$^+$ mCAF signal related to the spatial presence of cancer cells. Through analysis of clinical datasets spanning multiple tumor types, we are able to show that FAP$^+$ cells crowded the periphery of actual tumor nests in ring-like fashion. This is interesting as the strongest FAP$^+$ signal arises at the tumor margin that needs to be cleanly resected with a safety zone. We thus implemented machine learning segmentation approach to intraoperatively highlight different margin zones within 1 and 3 mm of the SOP-delineated tumor periphery.

Future work needed

While this work establishes the potential of FAP-based SOPs, there are several necessary steps to translate this technology clinically. Currently, most FGS probes are imaging in either far-red or near-infrared wavelengths. Designing and characterizing an FAP-based SOP in one of these spectral windows would allow for use on existing surgical fluorescence imaging systems (*51*). Working in these wavelengths would also potentially allow for the imaging of deeper tissue regions owing to reduced optical scattering at red-shifted wavelengths. On the basis of prior experience with fluorophores at blue-shifted wavelengths, the identification of a far-red SOP will likely require a thorough screen to identify a lead compound and likely involve longer staining times for agent diffusion to occur. The need for deeper imaging may be less relevant for FGS, where tissue shavings or resections are performed rapidly with the need to reassess margins continuously.

In addition to optimizing the fluorophore, it will also be important to consider the effects that the spray device has on staining performance. While we used a device sufficient for preclinical work, we expect that a custom clinical device will need to be implemented to account for the larger operative fields in human surgeries. Important factors to consider will be droplet size, density of droplets per unit area, and dispersion of the spray cloud. Each of these factors can be optimized on the basis of similar studies for nasal spray devices (*41*).

Another potential limitation of current FGS imaging probes—including the one used here—is that they are "always on." Alternatively, a probe that can be chemically or optically turned off may have unique applications to remove nonspecific signal from residual SOP and thus limit background. With iterative restaining in more complicated surgical resections, one would expect to see an increase in the signal intensity of background tissue, effectively lowering contrast with each subsequent restain. This could be alleviated with an erasable probe, ensuring a true return to baseline between imaging steps. There are several mechanisms to achieve turn-off probes, including photoreactive self-quenching dyes (*52*) and bioorthogonal chemical reactions that either cleave off the fluorescent dye or introduce a quencher to eliminate signal (*53*). All of these solutions can potentially be used for next-generation SOP probe design.

MATERIALS AND METHODS

Materials

All reagents and solvents were procured from Thermo Fisher Scientific or Sigma-Aldrich and used without further purification. Fibroblast activation protein inhibitor FAP-IN-2 trifluoroacetic acid (purity: 99.92%) and sodium alginate were purchased from MedChemExpress. The NHS ester of BODIPY-TMR, was purchased from Lumiprobe. All starting materials were reconstituted in dry dimethyl sulfoxide (DMSO) and used without further processing.

Synthesis of FTF-BODIPY-TMR

To a solution of BODIPY-TMR-NHS (5 mg, 10 μmol, 1 equiv) and FAP-IN-2 (12 mg, 20 μmol, 2 equiv) in anhydrous dimethylformamide (500 μl), *N*,*N*-diisopropylethylamine (25 μl, 144 μmol, 14.4 equiv) was added. The reaction mixture was stirred overnight at room temperature and then, immediately purified via preparative, reversed-phase high-performance LC (2 to 80% acetonitrile/H_2O with 0.1% formic acid added to both solvents) to afford >98% pure FTF-BODIPY-TMR as a pink powder (yield: 7.1 mg, 82%). ^{1}H NMR (400 MHz, DMSO) δ 9.10 (t, J = 6.1 Hz, 1H), 8.80 (d, J = 4.3 Hz, 1H), 8.24 (s, 2H), 7.97 (d, J = 9.2 Hz, 1H), 7.89 to 7.82 (m, 3H), 7.69 (s, 1H), 7.51 (d, J = 4.4 Hz, 1H), 7.43 (dd, J = 9.2, 2.7 Hz, 1H), 7.14 (d, J = 4.1 Hz, 1H), 7.04 to 6.97 (m, 2H), 6.69 (d, J = 4.1 Hz, 1H), 5.12 (dd, J = 9.3, 2.9 Hz, 1H), 4.39 to 4.28 (m, 1H), 4.27 to 4.20 (m, 2H), 4.13 (t, J = 6.6 Hz, 2H), 3.81 (s, 3H), 3.50 (s, 1H), 3.40 (d, J = 23.7 Hz, 4H), 2.87 (dd, J = 28.2, 13.3 Hz, 2H), 2.62 (t, J = 7.6 Hz, 2H), 2.54 (s, 1H), 2.44 (d, J = 12.6 Hz, 7H), 2.29 (dd, J = 12.2, 7.5 Hz, 3H), 2.22 (s, 3H), 1.92 (t, J = 7.0 Hz, 2H), 1.23 (s, 2H), 0.93 to 0.74 (m, 2H). MS(ESI$^+$): *m*/*z* calc'd for $C_{45}H_{48}BF_4N_8O_5$ $\{M + H\}^+$ = 867.38; found, $\{M + H\}^+$ = 867.78.

Characterization

Nuclear magnetic resonance

NMR spectra were recorded on a Bruker Avance UltraShield 400-MHz spectrometer. ^{1}H NMR chemical shifts are reported in ppm and were referenced internally with respect to residual protons (δ = 2.50 for DMSO-d6). Coupling constants are reported in hertz. NMR spectra processing and analysis were performed with MestReNova Research S.L (version 15.0.1).

Liquid chromatography–mass spectrometry

HPLC-MS analysis was performed on a Waters instrument equipped with a Waters 2424 ELS Detector, Waters 2998 UV-Vis Diode array Detector, Waters 2475 Multi-wavelength Fluorescence Detector, and a Waters 3100 Mass Detector. Separations used an HPLC-grade water/acetonitrile solvent gradient with an XTerra MS C18 Column, 125 Å, 5 μm, 4.6 mm–by–50 mm column; routine analyses were conducted with 0.1% formic acid added to both solvents.

Optical spectra

FTF-BODIPY-TMR was diluted to a concentration of 1 μM in DMSO. Absorbance and fluorescence spectra were performed with a multimode microplate reader (Tecan, Spark 500) using 96-well transparent bottom black polystyrene microplates (Corning). Absorption was measured from 400 to 700 nm in 1-nm steps for all compounds. All spectra were measured in triplicate, and the background was corrected from measurements of blank wells. Spectra were smoothed using a moving average filter with a smoothing factor of 0.01 and a window size of 5. All calculations were done in MATLAB 2023B (Mathworks, Natick, MA).

Toxicity

Twenty-four hours before treatment, NIH-3T3 cells were plated at 5000 cells per well in a 96-well plate. On the day of treatment, a 1:10 serial dilution of FTF-BODIPY-TMR was prepared spanning concentrations from 0.001 to 100 μM with a constant 1% DMSO concentration and applied to cells for 2 min. Following treatment, the cells were washed with media before incubating for 72 hours. After incubation, the cells were treated with a 10× dilution of Presto Blue (Thermo Fisher Scientific) and incubated for 60 min at 37°C. Absorbance measurements were performed at 570 nm in a multimode microplane reader (Tecan, Spark 500).

Cell culture

Cells were plated and cultured in Dulbecco's modified Eagle's medium (DMEM, Corning) supplemented with 10% fetal bovine serum (Corning) and 1% penicillin-streptomycin (Corning) at 37°C and 5% CO_2. Cells were passaged with 0.05% trypsin-EDTA (Corning). For all ex vivo stain optimization, 4T1 [American Type Culture Collection (ATCC), CRL-2539] murine mammary tumor cells were transfected with GFP as previously described (*54*). For validation of SOP-based margin detection, B16 F10 (ATCC, CRL-6475) and MC38 (gift from M. Smyth, CVCL_B288) were also transfected with GFP. KPCY pancreatic ductal adenocarcinoma cells (clone 2838c3) were acquired from Kerafast (EUP013-FP), and NIH 3T3 cells were acquired from ATCC (CRL-1658).

Mouse models

All animals were obtained from the Jackson Laboratory (stock # 000664 or # 000651) and housed under specific pathogen–free conditions at Massachusetts General Hospital. Experiments were approved by the MGH Institutional Animal Care and Use Committee (IACUC) and were performed according to MGH IACUC protocol 2013 N000157). All mice were provided ad libitum access to food and water and a standard 12-hour light/dark cycle. All experiments were performed under isoflurane gas anesthesia. Ten-week-old male/female C57BL/6J and BALB/C mice were used for all experiments. A total of $n = 60$ were mice used. This included $n = 20$ mice for probe optimization, $n = 15$ mice for ex vivo tumor imaging, $n = 20$ mice for confocal microscopy, and $n = 5$ mice for FGS.

Tumor model

For ex vivo B16 F10-GFP tumor imaging, 10^6 B16 F10tumor cells in 100 μl of serum-free DMEM were injected into the upper rear flanks of C57BL/6 mice. For ex vivo MC38 tumor imaging, 10^6 MC38 tumor cells in 100 μl of serum-free DMEM were injected into the upper rear flanks of C57BL/6 mice. For ex vivo 2838c3 tumor imaging, 10^6 2838c3 tumor cells in 100 μl of serum-free DMEM were injected into the upper rear flanks of C57BL/6 mice. For ex vivo 4T1 tumor imaging, 5×10^5 4T1 tumor cells in 100 μl of serum-free DMEM were injected into the fourth right mammary fat pad of female BALB/C mice. All tumor models were allowed to grow for 7 days before excision.

Human tissue collection

Tissue was collected under an institutional review board–approved protocol at the Massachusetts General Hospital (IRB 2019P002830) and is compliant with the Declaration of Helsinki and Health Insurance Portability and Accountability Act regulations. The eligibility criteria included adult patients with a clinical diagnosis of cancer who underwent image-guided biopsy of liver lesions for clinical reasons (disease progression or eligibility for other trial enrollments). Tumor samples from three patients were collected and analyzed.

Ex vivo tissue staining

Topical stain optimization

Excised tumors, liver, and adipose were embedded in 4% w/v agarose and cut into 300-μm sections using a vibrating microtome. Sections were fully submerged in 0.2-, 1-, 5-, or 25-μM solutions of FTF-BODIPY-TMR diluted in PBS for 1, 2, 5, or 10 min before a 5-min wash in PBS. Following imaging, tumor-to-background tissue ratios were calculated from the average fluorescence intensity of each tissue type. To optimize wash times, tissue sections were submerged in a 1 μM solution of FTF-BODIPY-TMR in PBS for 2 min before a 1-, 2-, 5-, or 10-min wash.

Spray formulation optimization

Spray performance was tested using a commercial spray device (MADomizer bottle; Teleflex). Excised tumors, liver, and adipose were embedded in 4% w/v agarose and cut into 300-μm sections using a vibrating microtome. Sections were then sprayed. Following staining, samples were continuously sprayed with PBS or PBS + EDTA (alginate condition only) for 5 min.

Whole preclinical tumor staining

Whole tumors were resected with either surrounding skin for subcutaneous tumors or adjacent mammary gland for mammary tumors. Tumor and peritumoral tissue were stained with the optimized SOP protocol: Pretreatment with 3% $CaCl_2$, 2-min stain with SOP-alginate, and followed by a 5-min wash with 3% EDTA.

Antibody staining

Fresh, whole-tissue antibody staining was performed following SOP staining. Fluorescently labeled antibodies were diluted to 10 μg/ml, and samples were stained for 10 min following a 5-min wash in PBS. Antibodies were obtained form BioXCell (αCD45: clone 104.2, catalog no. BE0300; αFAP: clone 73.3, catalog no. BE0374), and conjugated with AF647 Dye (Lumiprobe) using previously described methods (*55*) to achieve a degree of labeling of 2 to 4.

Clinical biopsy staining

Clinical biopsies were kept on ice before staining and were stained within 30 min of collection. Samples were treated with 3% $CaCl_2$ and then stained with SOP-alginate for 2 min, following 5 min of wash with a 3% EDTA solution. Biopsies were subsequently submerged in a 1 μg/ml solution of proflavine for 60 s followed by an additional 5 min wash in PBS.

Ex vivo wide-field epifluorescence imaging

Epifluorescence imaging for SOP optimization was performed with a commercially available preclinical OV-110 TM optical system (Olympus, Center Valley, PA) using a Hamamatsu C9100-13 EM-CCD camera (Hamamatsu, Bridgewater, NJ). This system enabled imaging of white light reflectance, GFP fluorescence signal (fluorescein isothiocyanate filter cube), and BODIPY-TMR signal [tetramethyl rhodamine isothiocyanate (TRITC) filter cube]. Integration times were set to 200, 500, and 500 ms for white light, GFP, and BODIPY-TMR images, respectively.

Confocal tissue imaging

Confocal imaging was performed using a customized Olympus FV1000 confocal microscope (Olympus America). A 2× [XLFluor, numerical aperture (NA) 0.14], a 4× (UPlanSApo, NA 0.16), and an XLUMPlanFL N 20× (NA 1.0) water immersion objective were used

for imaging (Olympus America). Tumor cells (B16 F10, 4T1, MC38, or 2838c3 -TagGFP), FTF-BODIPY-TMR, and Cy5-conjugated antibodies were excited sequentially using a 473-, a 555-, and a 647-nm diode laser in combination with a DM-405/488/559/635 nm dichroic beam splitter. Emitted light was further separated by beam splitters (SDM-473, SDM-560, and SDM-640) and emission filters BA430-455, BA490-540, BA575-620, and BA655-755 (Olympus America). Confocal laser power was optimized during each imaging session to avoid photobleaching, phototoxicity, or tissue damage.

Fluorescence-guided surgery

FGS was performed using a custom-built intraoperative imaging system using an epifluorescence intraoperative microscope with a 0.65-5 variable objective. Images were collected in white light, and TRITC channels (ex: 525; em: 585). On the day of imaging, mice bearing orthotropic 4T1 mammary tumors were anesthetized and positioned under the imaging system. The tumor was exposed by making three cuts to the abdominal skin: a midline cut followed by two transverse cuts above and below the tumor. Once exposed, background images were collected. The operative field was treated with 3% $CACl_2$ before staining with SOP-alginate for 2 min. After staining, the field was rinsed with 3% EDTA in PBS for 5 min. Fluorescence imaging was performed. On the basis of the results of tumor segmentation, tumor regions were resected. A second round of staining and imaging was performed to confirm complete removal of tumor.

RNA sequencing analysis of FAP expression in human tumors

The publicly available datasets were retrieved from the Gene Expression Omnibus from cited studies. Average FAP expression comparisons across cell types and tissue origins were performed using the in-house single-cell analysis pipeline scalpi (https://gitlab.com/pwirapati/scalpi). A logistic regression–based cell type classifier, trained on cellular annotations (*21*), was applied across datasets. Average FAP expression per cell type and tissue origin was computed using the scalpi_ac function and visualized as dot plots with mean expression levels indicated by horizontal lines using the ac_plot function in scalpi.

Visium HD Transcriptomics analysis

Publicly available Visium HD datasets were obtained from the 10x Genomics data portal. The platform captures whole-transcriptome profiles over a 6.5 mm–by–6.5 mm area at 2-μm resolution. Hierarchical clustering of RNA expression was performed at 8-μm bin resolution using Ward's method, implemented in the in-house nclust package (https://gitlab.com/pwirapati/nclust). Tumor cells and fibroblasts were annotated on the basis of canonical gene expression signatures. Spatial coordinates of tumor and fibroblast bins were used to compute relative distances via the in-house spati package (https://gitlab.com/pwirapati/spati). Fibroblast bins within 100 μm of the nearest tumor bin and those located ≥100 μm away were aggregated separately to calculate normalized average FAP expression levels. Differences in expression between proximity-based fibroblast groups were assessed using the Wilcoxon rank-sum test.

We performed spatial FAP expression analysis in a subset of 12 patients (fig. S10) to determine the spatial relationship of FAP-expressing cells to tumor cells. For each sample, the Euclidean distance of every fibroblast to the nearest tumor epithelial cell was computed from spatial coordinates using a nearest-neighbor distance function. Distances were discretized into 20-μm intervals, yielding nonoverlapping concentric distance bins spanning from the tumor boundary into the surrounding tissue. Each cell was assigned to a bin according to its maximum distance value. To evaluate FAP expression in fibroblasts, within each distance bin, the total FAP expression across fibroblasts was divided by an adjusted denominator consisting of the number of fibroblasts in that bin plus a pseudocount equal to the 0.5% of the global fibroblast pool. This correction penalized bins with very few fibroblasts, thereby stabilizing estimates of mean expression at the remote tumor periphery ends. The resulting bin-level FAP expression values were plotted as a continuous function of distance to visualize spatial trends

Image analysis

All image visualization was performed with Fiji (ImageJ, 2.14.0/1.54F). Images were automatically windowed and leveled to maximize contrast and false-colored to differentiate channels. Image analysis was performed with MATLAB 2023B (Mathworks, Natick, MA).

K-means clustering for margin detection

Images of four tumor types (B16 F10, MC38, 4T1, and 2838c3) were aggregated into a single histogram for *k*-means segmentation using the MATLAB function imsegkmeans with three clusters to determine the centroids for image segmentation. Centroids from the aggregated data were subsequently applied to each individual tumor type to determine tumor segmentation. Tumor margins were determined by performing a dilation of the tumor mask corresponding to the desired thickness (1 or 3 mm). To assess accuracy, binary masks were created from the GFP images using an Otsu's automatic threshold. Metrics for segmentation accuracy were calculated as follows: The Jaccard index was calculated as the ratio intersection of the SOP mask (A) and the GFP mask (B) over the union of the two

$$J(A,B) = \frac{|A \cap B|}{|A \cup B|}$$

Dice score was calculated as the ratio of true positives over the sum of true positives, false positives, and false negatives

$$Dice = \frac{2 \cdot TP}{2 \cdot TP + FP + FN}$$

Colocalization of SOP signal and anti-FAP or anti-CD45 antibody staining

Both images were filtered with a Gaussian filter with a 3 × 3 kernel to reduce noise. A binary mask of the cells in each image was generated from the anti-FAP image. First, morphological opening was performed using the imopen function and a four-pixel wide disk structuring element. The output image was then binarized using Otsu's method and the imbinarize function. This mask was applied to each image before generating a binned scatter plot with 250 bins along each axis. A linear fit for each dataset was performed and plotted using the built-in polyfit function with a degree of $n = 1$. A Pearson's correlation coefficient and R^2 value were calculated using built-in functions.

Statistics

All statistical data analyses were performed using GraphPad Prism 9 software, and results are expressed as means ± SD. For normally distributed datasets, we used two-tailed Student's *t* test and one-way analysis of variance (ANOVA) followed by Bonferroni's multiple

comparison test. When variables were not normally distributed, we performed nonparametric Mann-Whitney or Kruskal-Wallis tests. P values >0.05 were considered not significant (n.s.), P values <0.05 were considered significant.

Supplementary Materials

This PDF file includes:

Figs. S1 to S10

REFERENCES AND NOTES

1. C. D. Scopa, P. Aroukatos, A. C. Tsamandas, C. Aletra, Evaluation of margin status in lumpectomy specimens and residual breast carcinoma. *Breast J* **12**, 150–153 (2006).
2. R. Weissleder, C. H. Tung, U. Mahmood, A. Bogdanov, In vivo imaging of tumors with protease-activated near-infrared fluorescent probes. *Nat. Biotechnol.* **17**, 375–378 (1999).
3. L. J. Lauwerends, P. B. A. A. van Driel, R. J. Baatenburg de Jong, J. A. U. Hardillo, S. Koljenovic, G. Puppels, L. Mezzanotte, C. W. G. M. Löwik, E. L. Rosenthal, A. L. Vahrmeijer, S. Keereweer, Real-time fluorescence imaging in intraoperative decision making for cancer surgery. *Lancet Oncol.* **22**, e186–e195 (2021).
4. J. S. D. Mieog, F. B. Achterberg, A. Zlitni, M. Hutteman, J. Burggraaf, R. J. Swijnenburg, S. Gioux, A. L. Vahrmeijer, Fundamentals and developments in fluorescence-guided cancer surgery. *Nat. Rev. Clin. Oncol.* **19**, 9–22 (2022).
5. F. Azari, G. Kennedy, E. Bernstein, C. Hadjipanayis, A. Vahrmeijer, B. Smith, E. Rosenthal, B. Sumer, J. Tian, E. Henderson, A. Lee, Q. Nguyen, S. Gibbs, B. Pogue, D. Orringer, C. Charalampaki, L. Martin, J. Tanyi, M. Lee, J. Y. Lee, S. Singhal, Intraoperative molecular imaging clinical trials: A review of 2020 conference proceedings. *J. Biomed. Opt.* **26**, 050901 (2021).
6. K. Wang, Y. Du, Z. Zhang, K. He, Z. Cheng, L. Yin, D. Dong, C. Li, W. Li, Z. Hu, Fluorescence image-guided tumour surgery. *Nat. Rev. Bioeng.* **1**, 161–179 (2023).
7. P. Bou-Samra, N. Muhammad, A. Chang, R. Karsalia, F. Azari, G. Kennedy, W. Stummer, J. Tanyi, L. Martin, A. Vahrmeijer, B. Smith, E. Rosenthal, P. Wagner, D. Rice, A. Lee, A. Abdelhafeez, M. M. Malek, G. Kohanbash, W. Barry Edwards, E. Henderson, J. Skjøth-Rasmussen, R. Orosco, S. Gibbs, R. W. Farnam, L. Shankar, B. Sumer, A. T. N. Kumar, L. Marcu, L. Li, V. Greuv, E. J. Delikatny, J. Y. K. Lee, S. Singhal, Intraoperative molecular imaging: 3rd Biennial clinical trials update. *J. Biomed. Opt.* **28**, 050901 (2023).
8. P. A. Sutton, M. A. van Dam, R. A. Cahill, S. Mieog, K. Polom, A. L. Vahrmeijer, J. van der Vorst, Fluorescence-guided surgery: Comprehensive review. *BJS Open* **7**, zrad049 (2023).
9. J. L. Tanyi, L. M. Randall, S. K. Chambers, K. A. Butler, I. S. Winer, C. L. Langstraat, E. S. Han, A. L. Vahrmeijer, H. S. Chon, M. A. Morgan, M. A. Powell, J. H. Tseng, A. S. Lopez, R. M. Wenham, A phase III study of pafolacianine injection (OTL38) for intraoperative imaging of folate receptor-positive ovarian cancer (Study 006). *J. Clin. Oncol.* **41**, 276–284 (2023).
10. R. J. Deutsch-Williams, K. A. Schleyer, R. Das, J. E. Carrothers, R. H. Kohler, C. Vinegoni, R. Weissleder, FAP-targeted fluorescent imaging agents to study cancer-associated fibroblasts in vivo. *Bioconjug. Chem.* **36**, 44–53 (2024).
11. Y. Mori, E. Novruzov, D. Schmitt, J. Cardinale, T. Watabe, P. L. Choyke, A. Alavi, U. Haberkorn, F. L. Giesel, Clinical applications of fibroblast activation protein inhibitor positron emission tomography (FAPI-PET). *NPJ Imaging* **2**, 48 (2024).
12. Y. Nakamoto, S. Baba, H. Kaida, O. Manabe, T. Uehara, Recent topics in fibroblast activation protein inhibitor-PET/CT: Clinical and pharmacological aspects. *Ann. Nucl. Med.* **38**, 10–19 (2024).
13. A. Altmann, U. Haberkorn, J. Siveke, The latest developments in imaging of fibroblast activation protein. *J. Nucl. Med.* **62**, 160–167 (2021).
14. H. Hricak, M. E. Mayerhoefer, K. Herrmann, J. S. Lewis, M. G. Pomper, C. P. Hess, K. Riklund, A. M. Scott, R. Weissleder, Advances and challenges in precision imaging. *Lancet Oncol.* **26**, e34–e45 (2025).
15. A. A. Fitzgerald, L. M. Weiner, The role of fibroblast activation protein in health and malignancy. *Cancer Metastasis Rev.* **39**, 783–803 (2020).
16. Q. Gong, W. Shi, L. Li, X. Wu, H. Ma, Ultrasensitive fluorescent probes reveal an adverse action of dipeptide peptidase IV and fibroblast activation protein during proliferation of cancer cells. *Anal. Chem.* **88**, 8309–8314 (2016).
17. R. Mukkamala, S. D. Lindeman, K. A. Kragness, I. Shahriar, M. Srinivasarao, P. S. Low, Design and characterization of fibroblast activation protein targeted pan-cancer imaging agent for fluorescence-guided surgery of solid tumors. *J. Mater. Chem. B* **10**, 2038–2046 (2022).
18. A. K. Umar, M. Butarbutar, S. Sriwidodo, N. Wathoni, Film-forming sprays for topical drug delivery. *Drug Des. Devel. Ther.* **14**, 2909–2925 (2020).
19. M. Pilewskie, M. Morrow, Margins in breast cancer: How much is enough? *Cancer* **124**, 1335–1341 (2018).
20. A. Bassez, H. Vos, L. Van Dyck, G. Floris, I. Arijs, C. Desmedt, B. Boeckx, M. Vanden Bempt, I. Nevelsteen, K. Lambein, K. Punie, P. Neven, A. D. Garg, H. Wildiers, J. Qian, A. Smeets, D. Lambrechts, A single-cell map of intratumoral changes during anti-PD1 treatment of patients with breast cancer. *Nat. Med.* **27**, 820–832 (2021).
21. R. Bill, P. Wirapati, M. Messemaker, W. Roh, B. Zitti, F. Duval, M. Kiss, J. C. Park, T. M. Saal, J. Hoelzl, D. Tarussio, F. Benedetti, S. Tissot, L. Kandalaft, M. Varrone, G. Ciriello, T. A. McKee, Y. Monnier, M. Mermod, E. M. Blaum, I. Gushterova, A. L. K. Gonye, N. Hacohen, G. Getz, T. R. Mempel, A. M. Klein, R. Weissleder, W. C. Faquin, P. M. Sadow, D. Lin, S. I. Pai, M. Sade-Feldman, M. J. Pittet, CXCL9:SPP1 macrophage polarity identifies a network of cellular programs that control human cancers. *Science* **381**, 515–524 (2023).
22. J. H. Choi, B. S. Lee, J. Y. Jang, Y. S. Lee, H. J. Kim, J. Roh, Y. S. Shin, H. G. Woo, C. H. Kim, Single-cell transcriptome profiling of the stepwise progression of head and neck cancer. *Nat. Commun.* **14**, 1055 (2023).
23. A. Franken, M. Bila, A. Mechels, S. Kint, J. Van Dessel, V. Pomella, S. Vanuytven, G. Philips, O. Bricard, J. Xiong, B. Boeckx, S. Hatse, T. Van Brussel, R. Schepers, C. Van Aerde, S. Geurs, V. Vandecaveye, E. Hauben, V. Vander Poorten, S. Verbandt, K. Vandereyken, J. Qian, S. Tejpar, T. Voet, P. M. Clement, D. Lambrechts, $CD4^+$ T cell activation distinguishes response to anti-PD-L1+anti-CTLA4 therapy from anti-PD-L1 monotherapy. *Immunity* **57**, 541–558.e7 (2024).
24. T. Hirz, S. Mei, H. Sarkar, Y. Kfoury, S. Wu, B. M. Verhoeven, A. O. Subtelny, D. V. Zlatev, M. W. Wszolek, K. Salari, E. Murray, F. Chen, E. Z. Macosko, C. L. Wu, D. T. Scadden, D. M. Dahl, N. Baryawno, P. J. Saylor, P. V. Kharchenko, D. B. Sykes, Dissecting the immune suppressive human prostate tumor microenvironment via integrated single-cell and spatial transcriptomic analyses. *Nat. Commun.* **14**, 663 (2023).
25. N. Kim, H. K. Kim, K. Lee, Y. Hong, J. H. Cho, J. W. Choi, J. I. Lee, Y. L. Suh, B. M. Ku, H. H. Eum, S. Choi, Y. L. Choi, J. G. Joung, W. Y. Park, H. A. Jung, J. M. Sun, S. H. Lee, J. S. Ahn, K. Park, M. J. Ahn, H. O. Lee, Single-cell RNA sequencing demonstrates the molecular and cellular reprogramming of metastatic lung adenocarcinoma. *Nat. Commun.* **11**, 2285 (2020).
26. C. H. L. Kürten, A. Kulkarni, A. R. Cillo, P. M. Santos, A. K. Roble, S. Onkar, C. Reeder, S. Lang, X. Chen, U. Duvvuri, S. Kim, A. Liu, T. Tabib, R. Lafyatis, J. Feng, S. J. Gao, T. C. Bruno, D. A. A. Vignali, X. Lu, R. Bao, L. Vujanovic, R. L. Ferris, Investigating immune and non-immune cell interactions in head and neck tumors by single-cell RNA sequencing. *Nat. Commun.* **12**, 7338 (2021).
27. K. Pelka, M. Hofree, J. H. Chen, S. Sarkizova, J. D. Pirl, V. Jorgji, A. Bejnood, D. Dionne, W. H. Ge, K. H. Xu, S. X. Chao, D. R. Zollinger, D. J. Lieb, J. W. Reeves, C. A. Fuhrman, M. L. Hoang, T. Delorey, L. T. Nguyen, J. Waldman, M. Klapholz, I. Wakiro, O. Cohen, J. Albers, C. S. Smillie, M. S. Cuoco, J. Wu, M. J. Su, J. Yeung, B. Vijaykumar, A. M. Magnuson, N. Asinovski, T. Moll, M. N. Goder-Reiser, A. S. Applebaum, L. K. Brais, L. K. DelloStritto, S. L. Denning, S. T. Phillips, E. K. Hill, J. K. Meehan, D. T. Frederick, T. Sharova, A. Kanodia, E. Z. Todres, J. Jané-Valbuena, M. Biton, B. Izar, C. D. Lambden, T. E. Clancy, R. Bleday, N. Melnitchouk, J. Irani, H. Kunitake, D. L. Berger, A. Srivastava, J. L. Hornick, S. Ogino, A. Rotem, S. Vigneau, B. E. Johnson, R. B. Corcoran, A. H. Sharpe, V. K. Kuchroo, K. Ng, M. Giannakis, L. T. Nieman, G. M. Boland, A. J. Aguirre, A. C. Anderson, O. Rozenblatt-Rosen, A. Regev, N. Hacohen, Spatially organized multicellular immune hubs in human colorectal cancer. *Cell* **184**, 4734–4752.e20 (2021).
28. S. Salcher, G. Sturm, L. Horvath, G. Untergasser, C. Kuempers, G. Fotakis, E. Panizzolo, A. Martowicz, M. Trebo, G. Pall, G. Gamerith, M. Sykora, F. Augustin, K. Schmitz, F. Finotello, D. Rieder, S. Perner, S. Sopper, D. Wolf, A. Pircher, Z. Trajanoski, High-resolution single-cell atlas reveals diversity and plasticity of tissue-resident neutrophils in non-small cell lung cancer. *Cancer Cell* **40**, 1503–1520.e8 (2022).
29. Y. Wang, Y. Liang, H. Xu, X. Zhang, T. Mao, J. Cui, J. Yao, Y. Wang, F. Jiao, X. Xiao, J. Hu, Q. Xia, X. Zhang, X. Wang, Y. Sun, D. Fu, L. Shen, X. Xu, J. Xue, L. Wang, Single-cell analysis of pancreatic ductal adenocarcinoma identifies a novel fibroblast subtype associated with poor prognosis but better immunotherapy response. *Cell Discov.* **7**, 36 (2021).
30. X. Zhang, L. Peng, Y. Luo, S. Zhang, Y. Pu, Y. Chen, W. Guo, J. Yao, M. Shao, W. Fan, Q. Cui, Y. Xi, Y. Sun, X. Niu, X. Zhao, L. Chen, Y. Wang, Y. Liu, X. Yang, C. Wang, C. Zhong, W. Tan, J. Wang, C. Wu, D. Lin, Dissecting esophageal squamous-cell carcinoma ecosystem by single-cell transcriptomic analysis. *Nat. Commun.* **12**, 5291 (2021).
31. R. Zilionis, C. Engblom, C. Pfirschke, V. Savova, D. Zemmour, H. D. Saatcioglu, I. Krishnan, G. Maroni, C. V. Meyerovitz, C. M. Kerwin, S. Choi, W. G. Richards, A. De Rienzo, D. G. Tenen, R. Bueno, E. Levantini, M. J. Pittet, A. M. Klein, Single-cell transcriptomics of human and mouse lung cancers reveals conserved myeloid populations across individuals and species. *Immunity* **50**, 1317–1334.e10 (2019).
32. M. F. D. Oliveira, J. P. Romero, M. Chung, S. R. Williams, A. D. Gottscho, A. Gupta, S. E. Pilipauskas, S. Mohabbat, N. Raman, D. J. Sukovich, D. M. Patterson, Visium HD Development Team, S. E. B. Taylor, High-definition spatial transcriptomic profiling of immune cell populations in colorectal cancer. *Nat. Genet.* **57**, 1512–1523 (2025).
33. G. Lu, N. S. van den Berg, B. A. Martin, N. Nishio, Z. P. Hart, S. van Keulen, S. Fakurnejad, S. U. Chirita, R. C. Raymundo, G. Yi, Q. Zhou, G. A. Fisher, E. L. Rosenthal, G. A. Poultsides, Tumour-specific fluorescence-guided surgery for pancreatic cancer using panitumumab-

IRDye800CW: A phase 1 single-centre, open-label, single-arm, dose-escalation study. *Lancet Gastroenterol. Hepatol.* **5**, 753–764 (2020).
34. C. A. Metildi, S. Kaushal, M. Pu, K. A. Messer, G. A. Luiken, A. R. Moossa, R. M. Hoffman, M. Bouvet, Fluorescence-guided surgery with a fluorophore-conjugated antibody to carcinoembryonic antigen (CEA), that highlights the tumor, improves surgical resection and increases survival in orthotopic mouse models of human pancreatic cancer. *Ann. Surg. Oncol.* **21**, 1405–1411 (2014).
35. B. E. Schaafsma, J. S. D. Mieog, M. Hutteman, J. R. Van der Vorst, P. J. K. Kuppen, C. W. G. M. Löwik, J. V. Frangioni, C. J. H. Van de Velde, A. L. Vahrmeijer, The clinical use of indocyanine green as a near-infrared fluorescent contrast agent for image-guided oncologic surgery. *Ann. Surg. Oncol.* **104**, 323–332 (2011).
36. R. Pal, T. M. Lwin, M. Krishnamoorthy, H. R. Collins, C. D. Chan, A. Prilutskiy, M. P. Nasrallah, T. H. Dijkhuis, S. Shukla, A. L. Kendall, Fluorescence lifetime of injected indocyanine green as a universal marker of solid tumours in patients. *Nat. Biomed. Eng.* **7**, 1649–1666 (2023).
37. D. A. Novis, R. J. Zarbo, Interinstitutional comparison of frozen section turnaround time. A College of American Pathologists Q-Probes study of 32868 frozen sections in 700 hospitals. *Arch. Pathol. Lab. Med.* **121**, 559–567 (1997).
38. A. Loktev, T. Lindner, W. Mier, J. Debus, A. Altmann, D. Jäger, F. Giesel, C. Kratochwil, P. Barthe, C. Roumestand, U. Haberkorn, A tumor-imaging method targeting cancer-associated fibroblasts. *J. Nucl. Med.* **59**, 1423–1429 (2018).
39. T. A. Hope, J. Calais, A. H. Goenka, U. Haberkorn, M. Konijnenberg, J. McConathy, D. E. Oprea-Lager, L. Trimnal, E. Zan, K. Herrmann, C. M. Deroose, SNMMI Procedure Standard/EANM Practice Guideline for Fibroblast Activation Protein (FAP) PET. *J. Nucl. Med.* **66**, 26–33 (2025).
40. C. Kratochwil, P. Flechsig, T. Lindner, L. Abderrahim, A. Altmann, W. Mier, S. Adeberg, H. Rathke, M. Röhrich, H. Winter, P. K. Plinkert, F. Marme, M. Lang, H. U. Kauczor, D. Jäger, J. Debus, U. Haberkorn, F. L. Giesel, 68Ga-FAPI PET/CT: Tracer uptake in 28 different kinds of cancer. *J. Nucl. Med.* **60**, 801–805 (2019).
41. V. Kundoor, R. N. Dalby, Effect of formulation-and administration-related variables on deposition pattern of nasal spray pumps evaluated using a nasal cast. *Pharm. Res.* **28**, 1895–1904 (2011).
42. Y. Liao, L. Xie, J. Ye, T. Chen, T. Huang, L. Shi, M. Yuan, Sprayable hydrogel for biomedical applications. *Biomat. Sci.* **10**, 2759–2771 (2022).
43. W. Gao, J. C. Manning, K. Devaraj, R. R. Richards-Kortum, S. M. McFall, R. L. Murphy, A. Semeere, D. Erickson, Emerging trends in point-of-care technology development for oncology in low-and middle-income countries. *JCO Glob. Oncol.* **11**, e2500142 (2025).
44. R. Wang, R. J. Deutsch, E. D. Sunassee, B. T. Crouch, N. Ramanujam, Adaptive design of fluorescence imaging systems for custom resolution, fields of view, and geometries. *BME Front.* **4**, 0005 (2023).
45. P. Fozouni, S. Son, M. Díaz de León Derby, G. J. Knott, C. N. Gray, M. V. D'Ambrosio, C. Zhao, N. A. Switz, G. R. Kumar, S. I. Stephens, D. Boehm, C. L. Tsou, J. Shu, A. Bhuiya, M. Armstrong, A. R. Harris, P. Y. Chen, J. M. Osterloh, A. Meyer-Franke, B. Joehnk, K. Walcott, A. Sil, C. Langelier, K. S. Pollard, E. D. Crawford, A. S. Puschnik, M. Phelps, A. Kistler, J. L. DeRisi, J. A. Doudna, D. A. Fletcher, M. Ott, Amplification-free detection of SARS-CoV-2 with CRISPR-Cas13a and mobile phone microscopy. *Cell* **184**, 323–333.e9 (2021).
46. P. Gordon, V. P. Venancio, S. U. Mertens-Talcott, G. Coté, Portable bright-field, fluorescence, and cross-polarized microscope toward point-of-care imaging diagnostics. *J. Biomed. Opt.* **24**, 1–8 (2019).
47. R. A. Mustafa, N. Santesso, R. Khatib, A. A. Mustafa, W. Wiercioch, R. Kehar, S. Gandhi, Y. Chen, A. Cheung, J. Hopkins, B. Ma, N. Lloyd, D. Wu, N. Broutet, H. J. Schünemann, Systematic reviews and meta-analyses of the accuracy of HPV tests, visual inspection with acetic acid, cytology, and colposcopy. *Int. J. Gynecol. Obstet* **132**, 259–265 (2016).
48. P. Demétrio de Souza França, S. Kossatz, C. Brand, D. K. Zanoni, S. Roberts, N. Guru, D. Adilbay, A. Mauguen, C. V. Mayor, W. A. Weber, H. Schöder, R. A. Ghossein, I. Ganly, S. G. Patel, T. Reiner, A phase I study of a PARP1-targeted topical fluorophore for the detection of oral cancer. *Eur. J. Nucl. Med. Mol. Imaging* **48**, 3618–3630 (2021).
49. M. W. Dewhirst, T. W. Secomb, Transport of drugs from blood vessels to tumour tissue. *Nat. Rev. Cancer* **17**, 738–750 (2017).
50. N. M. Long, C. S. Smith, Causes and imaging features of false positives and false negatives on 18F-PET/CT in oncologic imaging. *Insights Imaging* **2**, 679–698 (2011).
51. A. V. DSouza, H. Lin, E. R. Henderson, K. S. Samkoe, B. W. Pogue, Review of fluorescence guided surgery systems: Identification of key performance capabilities beyond indocyanine green imaging. *J. Biomed. Opt.* **21**, 080901 (2016).
52. E. A. Halabi, R. Weissleder, Light-deactivated fluorescent probes (FLASH-Off) for multiplexed imaging. *J. Am. Chem. Soc.* **145**, 8455–8463 (2023).
53. M. Wilkovitsch, M. Haider, B. Sohr, B. Herrmann, J. Klubnick, R. Weissleder, J. C. T. Carlson, H. Mikula, A cleavable C_2-symmetrictrans-cyclooctene enables fast and complete bioorthogonal disassembly of molecular probes. *J. Am. Chem. Soc.* **142**, 19132–19141 (2020).
54. F. Pucci, C. Garris, C. P. Lai, A. Newton, C. Pfirschke, C. Engblom, D. Alvarez, M. Sprachman, C. Evavold, A. Magnuson, U. H. von Andrian, K. Glatz, X. O. Breakefield, T. R. Mempel, R. Weissleder, M. J. Pittet, SCS macrophages suppress melanoma by restricting tumor-derived vesicle-B cell interactions. *Science* **352**, 242–246 (2016).
55. J. Ko, M. Wilkovitsch, J. Oh, R. H. Kohler, E. Bolli, M. J. Pittet, C. Vinegoni, D. B. Sykes, H. Mikula, R. Weissleder, J. C. T. Carlson, Spatiotemporal multiplexed immunofluorescence imaging of living cells and tissues with bioorthogonal cycling of fluorescent probes. *Nat. Biotechnol.* **40**, 1654–1662 (2022).

Acknowledgments: We thank Y. Nguyen for culturing the KPCY 2838c3 cells. Cartoon schematics were created in part with BioRender. **Funding:** This work was supported by the CSB Development Fund and in part by the following NIH grants: R33CA277820 (R.W.), R01CA257623 (R.W.), T32CA079443 (R.W.), and R01CA281735 (R.W.). This work was supported in part by a donation to the Geneva Translational Oncology Program and the Fondation Privée of the Geneva University Hospitals (M.P.) and by the ISREC foundation (M.P.). **Author contributions:** Conceptualization: R.J.D.-W., J.C.T.C., M.P., and R.W. Data curation: R.J.D.-W. and Y.X. Formal analysis: R.J.D.-W., Y.X., Z.R., and C.V. Investigation: R.J.D.-W., Y.X., Z.R., M.G., P.W., and C.V. Methodology: all authors. Software: R.J.D.-W. and P.W. Validation: all authors. Supervision: J.C.T.C., M.P., and R.W. Visualization: R.J.D.-W., Z.R., and R.W. Writing—original draft: R.J.D.-W. and R.W. Writing—review and editing: R.W. and all coauthors. Funding acquisition: R.W. Project administration: R.W. Resources: R.W. **Competing interests:** The authors declare that they have no competing interests. **Data and materials availability:** All data needed to evaluate the conclusions in the paper are present in the paper and/or the Supplementary Materials. Publicly available Visium HD datasets were obtained from the 10x Genomics data portal and from the Gene Expression Omnibus (GEO) from cited studies (accession no. GSE28031).

Submitted 18 August 2025
Accepted 20 October 2025
Published 19 November 2025
10.1126/sciadv.aeb5810

Science Advances

Targeting cancer-associated fibroblasts for real-time intraoperative tumor identification with a spray-on fluorescent probe

Riley J. Deutsch-Williams, Yuxuan Xie, Zachary Rabinowitz, Marie Goemans, Pratyaksha Wirapati, Claudio Vinegoni, Jonathan CT Carlson, Mikael Pittet, and Ralph Weissleder

Sci. Adv. **11** (47), eaeb5810. DOI: 10.1126/sciadv.aeb5810